Two contractile pools of actomyosin distinctly load and tune E-cadherin levels during morphogenesis

Girish R. Kale[1], Xingbo Yang[2, 3], Jean-Marc Philippe[1], Madhav Mani[3], Pierre-François Lenne[1,*], Thomas Lecuit[1, 4,*]

1. Aix Marseille Université, CNRS, IBDM - UMR7288, 13009 Marseille, France.
2. Department of Molecular and Cellular Biology, Harvard University, Cambridge, MA 02138, USA
3. Northwestern University, 2145 Sheridan Road, Evanston, IL 60208, USA.
4. Collège de France, 11 Place Marcelin Berthelot, 75005 Paris, France.

* Authors for correspondance

Abstract

Epithelial tissues are highly dynamic. During embryonic morphogenesis cell contacts are constantly remodeled. This stems from active contractile forces that work against adhesive forces at cell interfaces. E-cadherin complexes play a pivotal role in this process as they both support inter-molecular adhesive forces and transmit mechanical tension due to their coupling to the cortical contractile actomyosin networks. In this context, it is unclear how tensile forces affect E-cadherin adhesion complexes and junction dynamics.

Addressing this calls for methods to estimate the tensile forces (load) experienced by adhesion complexes themselves. We address this during the early morphogenesis of the *Drosophila* embryonic ectoderm. Tensile forces generated by Myosin-II in the apico-medial cortex (medial Myosin-II) and in the junctional cortex (junctional Myosin-II) are responsible for junction remodeling. We combined mechanical inference and laser ablations to map tension at cell junctions. We also established Vinculin as a force sensor whose enrichment with respect to E-cadherin measures the load on adhesion complexes within each junction. Combining these tools, we show that the tension generated in both medial and junction pools of Myosin-II imposes load on E-cadherin adhesion complexes. Medial Myosin-II loads adhesion complexes uniformly on all junctions of a cell and increases levels of E-cadherin. Junctional Myosin-II, on the other hand, biases the distribution of the load between junctions of the same cell and exerts shear forces, which correspond to a decrease in the levels of E-cadherin. This work highlights the difference between medial Myosin-II and junctional Myosin-II in regulating E-cadherin levels during junction remodeling and suggest opposite effects of shear versus tensile stresses on E-cadherin complexes and on the dynamics of adhesive cell contacts.

Introduction

Tissue scale morphogenetic movements are driven by the dynamic remodeling of cell-cell adhesion and contractile actomyosin cytoskeleton at cell interfaces [1–4]. E-cadherin based cell adhesion machinery is not uniformly distributed at the cell interfaces. Within adherens junctions, E-cadherin forms *cis*- and *trans*-homophilic clusters whose size, density and lateral mobility (flow) depend, in part, on coupling to F-actin [5–7]. E-cadherin cell adhesion complexes are physically linked to the actomyosin cytoskeleton by α-Catenin and Vinculin, two F-actin binding proteins [8–13]. Such coupling to F-actin is essential for determining E-cadherin cluster size and number, underlying adhesion maturation, cell-cell cohesion [14,15], epithelial integrity *in vivo* [9] and cell sorting behavior [16]. Importantly, E-cadherin coupling to F-actin via α-Catenin is dependent on force: α-Catenin's interaction with F-actin can be modeled as a two-state catch bond, where force shifts the complex to a strongly bound-state [11] potentially by a tension-induced conformational change [10,17–20]. This argues that actomyosin-generated tension reinforces coupling to E-cadherin complexes *in vivo* [21,22]. By virtue of trans-homophilic interactions, E-cadherin complexes transmit these tensile forces across actomyosin cortices of neighboring cells [16]. The link between actomyosin contractility and E-cadherin may promote the regulation of cell adhesion by actomyosin contraction during tissue morphogenesis, though this possibility has not yet been directly addressed in a developmental context.

E-cadherin based cell adhesion plays a dual role by both maintaining tissue cohesion and by facilitating tissue remodeling under biochemical and mechanical regulation [23–26]. Contractile forces can affect cell adhesion, as they can directly influence the recruitment or turnover of E-cadherin molecules [27]. However, the evidence is sometimes contradictory, in some instances tension stabilizes E-cadherin, while in others tension appears to have the opposite effect. Mammalian cell culture experiments have demonstrated that cells respond to cell extrinsic tensile forces through local reorganization of F-actin cytoskeleton and increased recruitment or stabilization of E-cadherin [12,13,18,20]. However, other experiments have demonstrated that E-cadherin levels are reduced due to signaling downstream of Src and that the contractile activity of Myosin-II is the transducer of this reduction [28]. In addition, higher junctional tension correlates with increased turnover rate of E-cadherin molecules in MDCK cells [29], which in turn depends on the endocytosis/exocytosis of E-cadherin [30], arguing for tension reducing E-cadherin levels. Whether mechanical load regulates E-cadherin based adhesion *in vivo* has been comparatively little explored [31,32].

We addressed whether Myosin-II controls E-cadherin levels at cell contacts in the *Drosophila* early embryonic ectoderm, during its convergent-extension movements [33]. These movements rely on cell intercalation, which involves disassembly of junctions oriented along the dorsal-ventral axis (DV, vertical junctions) of the embryo, followed by elongation of new junctions along the anterior-posterior axis (AP, transverse junctions) [34–36]. Ectodermal cells have two distinctly regulated pools of Myosin-II that are both responsible for persistent junction shrinkage [37,38]. First, a pulsatile pool of medial Myosin-II produces semi-periodic contractions in the apical cortex, and junctional Myosin-II produces anisotropic contractions along vertical junctions. It is believed that these two networks cumulatively generate polarized tension at cell junctions. Indeed, tension at cell junctions is planar polarized as measured by focal laser ablation of actomyosin cortices [39] and by optical tweezers [40]. However, the measured tension is defined at the scale of a whole junction. It is unclear how this junction-level tension translates at the level of E-cadherin molecules to which actomyosin networks are coupled.

Further, it is unknown whether the respective actomyosin contraction contributions from the medial and the junctional networks is transmitted to E-cadherin molecules in a different manner. Lastly, it remains unresolved whether the impact of the respective contributions of the medial and junctional actomyosin on E-cadherin recruitment is distinct.

In this study, we have sought to investigate the effect of actomyosin contractility on cell adhesion, through the analysis of the load exerted onto E-cadherin. We analyzed the contribution of medial and junctional actomyosin networks to the load on adhesion complexes and to the recruitment of E-cadherin during morphogenesis of the embryonic ectoderm. Our analysis leads us to consider the differential role of tensile and shear stresses exerted respectively by the medial and junctional actomyosin networks.

Results

Drosophila Vinculin is recruited at adhesion complexes via α-Catenin in a Myosin-II dependent manner

In mammalian cells, Vinculin is recruited at E-cadherin adhesion complexes via its binding with α-Catenin [10,12,19]. We asked whether a similar phenomenon occurs in *Drosophila* embryonic ectoderm. We first verified that Vinculin is a component of E-cadherin-based adhesion complexes. Figure 1A shows E-cadherin clusters (arrowheads) co-localizing with Vinculin clusters. This point is qualitatively supported by the similarities in the intensity profiles for Vinculin and E-cadherin in a zoom-in view of a junction (Fig. 1B). To test whether α-Catenin is required for the recruitment of Vinculin to adhesion complexes, we injected embryos with double-stranded RNA (dsRNA) to achieve an RNAi mediated knockdown of α-Catenin (see Methods). α-Catenin knockdown significantly reduced Vinculin density at cell-cell contacts (Fig. 1C, C'), implying that α-Catenin is the primary interactor of Vinculin and facilitates Vinculin recruitment in adhesion complexes. Further, Vinculin was enriched in the apico-lateral domain of ectodermal cells similar to E-cadherin and Myosin-II (Supplementary Fig. 1A-D). With these observations, we conclude that Vinculin is a *bona fide* component of adhesion complexes in *Drosophila,* similar to its mammalian homologs.

We observed that Vinculin was enriched on vertical junctions compared to transverse junctions in the embryonic ectoderm (Supplementary Fig. 1H, H'). This distribution strikingly mirrored that of Myosin-II (Supplementary Fig. 1G, G'), which is known to be planar polarized [34,41,42]. This is remarkable since E-cadherin, however, is present at a lower concentration on vertical junctions [35,43]. Thus, Vinculin distribution was opposite to that of E-cadherin or α-Catenin, which are enriched on transverse junctions relative to vertical junctions (Supplementary Fig. 1E-F'). Vinculin planar polarized distribution was lost in the absence of α-Catenin (Fig. 1C’’). These results suggest a differential role of adhesion and contractility in regulating Vinculin recruitment and distribution.

The tensile forces generated by Myosin-II are known to produce structural changes in α-Catenin that expose a cryptic binding site for Vinculin and enhance the recruitment of Vinculin to adhesion complexes [10,18,19]. Thus, inhibiting Myosin-II activity can result in a reduction in the junctional recruitment of Vinculin. We tested this idea by injecting in embryos a Rok inhibitor, to block the Myosin-II activity (see Methods). Rok inhibition significantly reduced Myosin-II recruitment at junctions and abolished its planar polarity (Fig. 1D-D''). The same treatment also reduced Vinculin line densities on all junctions (Fig. 1E, E'). Noticeably, it inverted the

planar polarized distribution of Vinculin, which became similar to that of E-cadherin (Fig. 1E''). Rok inhibition also reduced E-cadherin density at junctions and amplified its planar polarity (Fig. 1F-F''). Given that Vinculin co-localizes with E-cadherin, we asked if the inversion of Vinculin planar polarity was due to a constitutive localization of Vinculin to E-cadherin in the absence of Myosin-II activity. When we normalized junctional Vinculin density to that of E-cadherin, the Vinc/E-cad ratio, indeed, this ratio was reduced upon Rok inhibition and its planar polarity was lost (Fig. 1G-G'') in a manner similar to Myosin-II. The fact that the planar polarity of Vinc/E-cad ratio qualitatively parallels that of Myosin-II suggests that the recruitment of Vinculin to adhesion complexes is enhanced by Myosin-II activity.

We further tested this by calculating the linear correlation coefficient between junctional Vinculin intensity and E-cadherin intensity. The correlation was performed by binning junctions according to their length. We term it the 'conditional correlation' (see Methods and Supplementary Fig. 2A). Such a measurement avoids the indirect correlation between the mean junctional intensities, as they are proportional to the inverse of junctional length. The correlation was consistently strong in Rok inhibited embryos independent of junction length (Supplementary Fig. 2B and C), indicating a constitutive association between Vinculin and E-cadherin in the absence of Myosin-II activity. In the presence of Myosin-II activity, the correlation between Vinculin and E-cadherin intensities was stronger on shorter junctions (Supplementary Fig. 2B and C). This suggests that Myosin-II activity enhances Vinculin recruitment to adhesion complexes at shrinking junctions.

Taken together, these results indicate that Vinculin is recruited to adhesion complexes at low levels independent of Myosin-II activity. In the presence of Myosin-II activity, Vinculin recruitment is enhanced further. In light of these observations, we decided to normalize Vinculin intensity (line density) with that of E-cadherin to specifically focus on the Myosin-II activity-dependent recruitment of Vinculin to E-cadherin.

The ratio of Vinculin to E-cadherin densities correlates with junctional tension

We then tested if Vinculin can be used as a molecular force sensor, as the recruitment of Vinculin can be an indicator of force dependent structural changes in α-Catenin. Such function is postulated for *Drosophila* Vinculin [31,44], but has not been demonstrated using explicit tension estimates. We have shown that Vinc/E-cad ratio, a measure of Vinculin enrichment relative to E-cadherin, has a distribution that correlates with that of junctional Myosin-II. Thus, we further asked if this ratio can be used to infer the tension on junctions, which, in turn, is generated by Myosin-II activity. First, we analyzed junctional tension by following relaxation kinetics of the junction after laser ablation (Fig. 2A, also see Methods). The post-ablation recoil velocity of the ablated junction has been used previously as a proxy for tension on junctions [37,39,45–47]. We measured the correlation between recoil velocities and either the junctional Myosin-II density or Vinc/E-cad ratio, and both quantities showed a statistically significant correlation (Fig. 2B and C). It is interesting to note that the recoil velocity has similar extent of correlation with Myosin-II as with Vinc/E-cad ratio, arguing for this ratio being a good proxy for junctional tension. Further, the correlation between recoil velocity and Vinc/E-cad ratio is stronger and more statistically significant as compared to the correlation between recoil velocity and Vinculin density itself (Supplementary Fig. 3A). This indicated that Vinc/E-cad ratio correlates better with the junctional tension, as compared to Vinculin intensity itself. Finally, there was

no correlation between the recoil velocity and E-cadherin density (Supplementary Fig. 3B), indicating the specificity of the analysis.

Laser ablation is an invasive method of tension estimation and suffers greatly from the difficulty to obtain very large data sets. The number of data points per embryo is limited, as the ablations are performed within a 10-minute time window during embryonic development and need to be done one junction at a time (see Methods). To overcome these limitations, we implemented a mechanical inference method to estimate junctional tensions [48–50] and correlated them with Myosin-II intensity and Vinc/E-cad ratio at a cellular level for thousands of cells across multiple embryos (see Methods) in a non-invasive, high-throughput manner. Figure 2D shows a snapshot from a wild type embryo on which we implemented the mechanical inference. Figure 2E shows the corresponding output of inferred tension from mechanical inference, where the thickness of the junction is proportional to the inferred tension. Note that the mechanical inference captures the tension cables along vertical junctions, which are reported to be under higher tension [39,46]. The planar polarity of inferred tension showed a trend similar to that of Vinc/E-cad ratio (Fig. 2F, G).

We calculated the linear correlation between Vinc/E-cad and inferred tension by binning junctions according to cell. We term it the 'local correlation' (see Methods and Supplementary Fig. 2A), which accounts for temporal and inter-embryo variations. This allowed us to combine data for all cells across multiple time points from many embryos (n≥5 embryos) to perform high-throughput statistics and gave us access to information at a cellular level. Figure 2H shows the distribution of the local correlation coefficient of junctional Myosin-II intensity and inferred tension. The median correlation coefficient for wild-type embryos is 0.6 and drops to 0.2 for Rok inhibited embryos. This showed that the inferred tension strongly correlates with Myosin-II activity, validating the mechanical inference once again. We performed the same analysis for Vinc/E-cad ratio and Vinculin intensity. Figure 2I shows the distribution of the local correlation coefficient of the Vinc/E-cad ratio and inferred tension. The median correlation coefficient for the wild-type embryos is 0.6 and drops to 0.14 after Rok inhibition, showing that Vinc/E-cad ratio strongly correlates with junctional tension in the presence of Myosin-II activity. Figure 2I shows the distribution of the local correlation coefficient of the Vinculin intensity and inferred tension. Even though the median correlation coefficient for the wild-type embryos is 0.56, the correlation is negative (-0.25) for Rok inhibited embryos. This is consistent with the inversion of Vinculin planar polarized distribution upon Rok inhibition (Fig. 1E''). This indicated, once again, that Vinc/E-cad ratio correlates better with tension as compared to Vinculin intensity itself.

Further, we estimated the 'conditional correlation' between inferred tension and junctional intensities. In such analysis, we showed that Vinc/E-cad ratio and Myosin-II intensity correlate better with inferred tension than does Vinculin intensity (Supplementary Fig. 4B and C). This observation is consistent with the laser ablation analysis, where we found that the estimated tension has a stronger correlation with Vinc/E-cad ratio or Myosin-II density as compared to Vinculin density itself (Fig. 2B, C and Supplementary Fig. 3A). This further established Vinc/E-cad as a better indicator of junctional tension than Vinculin intensity alone.

Altogether, our data indicated that Vinculin is a *bona fide* force sensor at adhesion complexes in *Drosophila* and that the distribution of Vinc/E-cad ratio can be used as a proxy for the distribution of junctional tension.

The ratio of Vinculin to E-cadherin densities reflects mechanical load on adhesion complexes
Mechanical inference and laser ablations provide an estimate for the junctional tension, a macroscopic quantity that is assumed to be uniform along the junction. E-cadherin adhesion complexes, on the other hand, are distributed in clusters along the junction (Fig. 1A and Supplementary Fig. 1E, F). Adhesion complexes, composed of E-cadherin, β-Catenin and α-Catenin, mechanically resist the contractile forces from actomyosin. Thus, adhesion complexes could be under differently oriented contractile forces and resist different magnitude of mechanical loads as they couple independently to the actomyosin network. Vinculin can be an estimate of the mechanical load [I still find this word confusing. By tensile forces on an a complex do we mean the load along the length of the complex. If so, we should state that clearly] experienced by each adhesion complex, as individual molecules of Vinculin are recruited to α-Catenin, in a load dependent manner [17,51]. Given that Vinc/E-cad ratio correlates with 'junctional tension' (a macroscopic quantity), we asked if it can be a readout of the mechanical load at adhesion complexes (a microscopic quantity), potentially providing access to forces at a sub-junctional level.

We address this question by over-expressing E-cadherin to increase its junctional level. The E-cadherin over-expression is expected to reduce the number of Myosin-II molecules per E-cadherin molecule, thereby reducing the load per adhesion complex. Vinculin level is hence expected to decrease relative to E-cadherin due to a reduction of tension supported by each E-cadherin molecule in the adhesion clusters (Fig. 3A). Indeed, E-cadherin over-expression produced a mild, but significant, increase in its junctional density (Fig. 3B, B'), while the distribution of Myosin-II was unchanged (Fig. 3E-E''). The junctional tension was also unchanged as shown by recoil velocities after laser ablations (Supplementary Fig. 5A). Concomitantly, there was a reduction in Vinculin density on all junctions (Fig. 3C, C''), leading to an even stronger decrease in Vinc/E-cad ratio (Fig. 3D, D'). We suggest that the decrease in Vinculin levels is not due to junctional tension or Myosin-II, as both quantities are unaffected by E-cadherin over-expression, but a response to the decrease of the load per adhesion complex (see Fig. 3A).

Moreover, Vinc/E-cad ratio can be calculated at a sub-junctional scale, even at a scale as small as individual adhesion clusters. Therefore, we further asked if we can see a consistent change in Vinc/E-cad ratio at a sub-junctional scale. Pixels in an image are the smallest possible spatial scale available in our analysis. So, we estimated Vinc/E-cad ratio at individual pixels (see Methods and Supplementary Fig. 6). In such an analysis, we observed a consistent reduction in Vinc/E-cad ratio upon E-cadherin over-expression, across all E-cadherin pixel intensity bins (Fig. 3F).

These quantifications suggest that, Vinc/E-cad ratio at each adhesion complex can be used as a proxy for the 'load on adhesion complex'. We note that Vinc/E-cad is independent of junctional length, thus can be estimated at a microscopic scale of adhesion clusters and will act as a molecular force sensor.

Medial and junctional Myosin-II distinctly load E-cadherin adhesion complexes

E-cadherin adhesion complexes are mechanically coupled to two spatially separated and distinctly regulated pools of Myosin-II, the medial pool and the junctional pool [37,52]. The relaxation kinetics of actomyosin cortex in laser ablation experiments suggest that medial Myosin-II exerts tension that is predominantly orthogonal to cell contacts, whereas junctional Myosin-II exerts tension that is predominantly parallel to cell contacts [37,39,43]. The forces produced by these two pools are differently oriented towards the junctions, so we asked whether they distinctly load adhesion complexes. First, we inhibited Myosin-II activity globally (Rok inhibition). This treatment reduced the levels of Vinc/E-cad ratio, and suppressed its planar polarity (Fig. 4A-B'), consistent with the idea that Myosin-II activity is required to load the adhesion complexes. Next, we tuned the Myosin-II activation in the medial pool only. A recent study demonstrated that a Gα12/13-RhoGEF2-Rho1-Rok pathway phosphorylates and activates Myosin-II in the medial pool downstream of GPCR signaling [38]. Using RhoGEF2-RNAi, we reduced the activation of Myosin-II only in the medial pool, without affecting Myosin-II recruitment in the junctional pool (Fig. 4C-C''). This treatment decreased the Vinc/E-cad ratio without affecting its planar polarized distribution (Fig. 4D, D'). This reduction in the Vinc/E-cad ratio could be due to a reduction of the load generated by the medial Myosin-II or a global reduction in junctional tension itself. We ruled out the latter possibility by laser ablation experiments (Supplementary Fig. 5B) and the fact that junctional Myosin-II intensity is unchanged in RhoGEF2-RNAi embryos (Fig. 4C”). To complement this observation, we increased the recruitment of Myosin-II in the medial pool using Gα12/13 over-expression, without affecting Myosin-II recruitment in the junctional pool (Fig. 4E-E''). Consistently, this treatment increased the Vinc/E-cad ratio without affecting its planar polarized distribution (Fig. 4F, F').

Thus, a global decrease (increase) in the levels of medial Myosin-II decreases (increases) the load on adhesion complexes uniformly on all junctions of a cell, as indicated by the uniform decrease (increase) of Vinc/E-cad ratio. In contrast to a global inhibition of Myosin-II activity, a specific inhibition of medial Myosin-II activity did not affect the planar polarized distribution of the junctional Myosin-II and preserved the planar polarized distribution of Vinc/E-cad ratio (Fig. 4B’, D’). Thus, we conclude that the planar polarized junctional Myosin-II imposes a larger amount of load on vertical junctions than transverse junctions and determines the planar polarity of Vinc/E-cad ratio.

Medial and junctional Myosin-II have opposite effects on junctional E-cadherin concentration

Given that medial and junctional pools of Myosin-II load adhesion complexes differently, we asked whether these two pools had distinct impacts on E-cadherin levels at cell junctions. We found that a global inhibition of Myosin-II activity (Rok inhibition) decreased the E-cadherin density at junctions (Fig. 1F, F'). Interestingly, a specific inhibition of the medial Myosin-II using RhoGEF2-RNAi without perturbation of the junctional Myosin-II (Fig. 4C-C’’) leads to a reduction in E-cadherin levels (Fig. 5A, A') that is comparable to the Rok inhibited embryos. This indicated that the global levels of E-cadherin are regulated by medial Myosin-II and the presence of junctional Myosin-II alone did not restore the global levels of E-cadherin. To further test this, we increased the levels of medial Myosin-II using Gα12/13 over-expression while preserving the levels of junctional Myosin-II (Fig. 4E-E’’). We observed an increase in E-

cadherin density at junctions (Fig. 5B-B'). These results suggest that the contractile medial Myosin-II regulates the global junctional recruitment of E-cadherin.

Planar polarized junctional Myosin-II (Supplementary Fig. 1G') is important for junction shrinkage [34,41]. It is hypothesized that the shear stress generated by junctional Myosin-II may affect the stability of adherens junctions by stretching the trans-cellular E-cadherin dimers [48]. However, this hypothesis has never been tested with experimental data due to the difficulty of measuring shear stress. Mechanical inference provides a unique way to approximate junctional shear stress from inferred tensions (Fig. 6A) [48]. Hence, we tested this hypothesis by estimating the 'conditional correlation' of E-cadherin density with inferred shear stress on junctions. The shear stress displayed a negative correlation with E-cadherin density on vertically shrinking junctions (Fig. 6C, D). In contrast, this correlation is reduced when pooling all junctions with different orientations (Fig. 6B) and vanishes for transverse junctions and Rok inhibited embryos (Fig. 6E, F). It is interesting to note that the transverse junctions show the same extent of this correlation, irrespective of Myosin-II activity. This further emphasizes that the shear forces are specifically active on vertical junctions. In addition, the correlation with inferred tension is much weaker (Fig. 6B, C, D). Combined together, these results indicate that shear stress rather than tension enhances the dissociation of E-cadherin from vertically shrinking junctions by shearing the adhesion complexes during junction remodeling.

Together these experiments suggest that the medial Myosin-II increases the levels of junctional E-cadherin by uniformly loading the adhesion complexes on cell junctions, while planar polarized junctional Myosin-II regulates junction remodeling by exerting shear forces on the adhesion complexes at vertically shrinking junctions.

Discussion

How contractile forces generated by Myosin-II activity regulate junction remodeling during morphogenesis is still an open question. In this study, we have used Vinculin as a molecular force sensor on E-cadherin complexes, whose recruitment to adhesion complexes is modulated by the contractile activity of Myosin-II and the resulting tensile forces; hence its ratio with E-cadherin provides a potential readout of mechanical forces on E-cadherin adhesion complexes at cell junctions. Using mechanical inference and laser ablation, we found that the enrichment of Vinculin relative to E-cadherin can be used to estimate the distribution of load on E-cadherin at cell junctions. While we have established Vinc/E-cad ratio as a tension sensor, it remains to be determined how this ratio depends on junctional tension explicitly. The conditional correlation revealed a length-dependent correlation between Vinc/E-cad ratio and inferred tension, with reduced correlation for short and long junctions (Supplementary Fig. 4C). This could suggest a non-linear dependence of Vinc/E-cad ratio on junctional tension with saturated response at short junctions under large tension and the presence of a tension threshold for activation at long junctions under small tension. Experiments with quantitatively controlled tension could determine the response curve of Vinc/E-cad ratio to the magnitude of tension.

Next, we tuned the loading forces on adhesion complexes by increasing the E-cadherin levels and revealed that Vinc/E-cad ratio can be a load sensor at the adhesion complex scale. Given that the stoichiometry between Vinculin and E-cadherin (proportional to Vinc/E-cad ratio) is a dimensionless quantity, we argue that the Vinc/E-cad ratio estimates the load experienced by

individual (diffraction limited) adhesion clusters. It is interesting to note that the distribution of Vinc/E-cad ratio is not homogeneous along a junction (e.g. Fig. 1G, 2D, 3D, 4B, 4D and 4F) and that Vinc/E-cad ratio is greater at brighter E-cadherin pixels (Fig. 3F). This indicates that load distribution is inhomogeneous along the junction and that the junctional subdomains with higher E-cadherin density experience greater load. This observation is consistent with a recent study [53], which reported that the mechanosensitive conformational changes in α-Catenin can be observed predominantly in larger E-cadherin clusters.

We used Vinc/E-cad ratio as a load estimate to study the effect of contractile forces from two distinct pools of Myosin-II, the medial and the junctional pool. The two pools are distinct in terms of their upstream regulation and have been studied in the *Drosophila* embryonic ectoderm [38]. They are mechanically coupled to adhesion complexes to exert forces on cell-cell contacts. In this study, we showed that these two pools of Myosin-II have distinct impact on the distribution of load on E-cadherin. Medial Myosin-II uniformly loads adhesion complexes across all junctions within a cell. In contrast, the planar polarized junctional Myosin-II biases the load towards vertical shrinking junctions, thus regulating the planar polarity of load. We have quantitatively demonstrated that both pools of Myosin-II exert forces on E-cadherin complexes and cell contacts.

The load generated due to activity of medial Myosin-II increases the levels of junctional E-cadherin. This observation is consistent with a study in the *Drosophila* mesoderm [32], where it is observed that the activity of medial Myosin-II protects E-cadherin from a Snail mediated downregulation. A change in junctional Rho signaling can also change E-cadherin levels through its impact on the F-actin organization and Myosin-II activity [54–56]. We think that this is not the case as the junctional Myosin-II levels and presumably junctional Rho signaling is unchanged when we specifically tuned medial Myosin-II. In fact, the changes in junctional E-cadherin levels correlated with the changes in medial Rho signaling downstream of activation by the Gα12/13-RhoGEF2 signaling module. Given that the inhibition of medial Rho signaling (RhoGEF2-RNAi) and Rok inhibition have similar impact on E-cadherin levels, we argue that the effect of medial Rho signaling on E-cadherin levels is through its effect on Myosin-II activation. It remains to be determined if the effect of medial Myosin-II activity on the levels of junctional E-cadherin is a mechanosensitive response or not.

We used a correlative analysis with mechanical inference to study the effect of junctional Myosin-II on junctional E-cadherin levels. We constructed a model to estimate shear stress based on inferred tensions. In this model, an asymmetric distribution of inferred tension on opposite sides of the junction generates shear stress that stretches E-cadherin trans-dimers on shrinking junctions [48]. Strikingly, we observed a negative correlation between the inferred shear stress and the junctional E-cadherin levels. Particularly, the negative correlation was specific to vertical junctions (the category to which shrinking junctions belong) and vanished on either the transverse junctions or the junctions from Rok inhibited embryos. This observation argues that junctional Myosin-II promotes dissociation of E-cadherin on vertically shrinking junctions during junction remodeling via a shear effect on E-cadherin complexes. However, we cannot rule out the possibility that medial Myosin-II also contributes to the shear stress to some extent, as the mechanical inference does not specify the source of the forces.

We hereby propose a mechanical model for cell junction remodeling, where we highlight the importance of the subcellular origin of contractile forces and their mechanical effect, namely tensile versus shear stress, in promoting a change in the levels of E-cadherin at cell contacts and on junction dynamics. The mechanisms that generate the different responses in E-cadherin levels remain unknown. We have established Vinculin as a molecular force sensor, but it remains to be determined whether Vinculin is involved in the stabilization of adherens junctions by regulating E-cadherin levels as a mechanotransducer. Vinculin is not essential for survival in *Drosophila* [57], raising questions about the necessity of its function as a mechanotransducer. To reveal the mechanism by which actomyosin contractility regulates E-cadherin levels, it is essential to study the magnitude and orientation of contractile forces, the spatial distribution of mechanical coupling between the adhesion complexes and the actomyosin network, and the different modes of energy dissipation at adhesive complexes under mechanical forces. Given this distinction between tensile and shear stress in the regulation of E-cadherin at cell contacts, it will also be important to consider the dynamics of E-cadherin complexes.

We speculate that adhesion mediated by E-cadherin has evolved to stabilize complexes under tensile stress and to constantly remodel them under shear stress. Tensile (i.e. normal) stresses reinforce cell-cell coupling to induce tissue deformation such as tissue invagination. This mode maintains adhesion below a threshold where junctions may collapse at once: this condition is observed when adhesion is mildly compromised using partial knock-down of E-cadherin or α-catenin in the mesoderm and endoderm where medial Myosin-II accumulates at very high levels. The shear mode also maintains adhesion but dynamically, thereby allowing tissue remodeling such as during cell intercalation in the ectoderm: on average the density of complexes could remain constant but the turnover of homophilic bonds would be increased. The differential effect of tensile and shear stress on E-cadherin dynamics has the potential of reconciling conflicting evidence on the role of contractile forces on adhesion and to open a study of energy dissipation at E-cadherin adhesion complexes in the study of cell-cell adhesion[4].

Methods

Fly lines and genetics

Vinculin-GFP and *Vinculin-mCherry* are fluorescently tagged transgenes of Vinculin. Vinculin gene was tagged at its N-terminus with either superfolder GFP or mCherry, using a pFlyFos025866 Fosmid which encompasses the 8kb of Vinculin gene along with 23.4kb upstream and 6.8kb downstream regions modified by Recombineering [58]. Tagged Fosmids were inserted in the genome at attp2 or attp40 landing sites, respectively using PhiC31 mediated site specific insertion transgenesis (Transgenesis performed by BestGene, Inc.).
E-cadherin-GFP is a homozygote viable DE-cadherin knock-in at the locus [59]. It is mostly used in combination with either MyoII-mCherry or Vinculin-mCherry. The combination with MyoII-mCherry is used to quantify the localization of Myosin-II and E-cadherin. The combination with Vinculin-mCherry is used to localization of Vinculin and to estimate Vinc/E-cad ratio.
MyoII-mCherry and *MyoII-GFP* are tagged constructs of *Drosophila* Myosin-II regulatory light chain encoded by gene *spaghetti squash* (*sqh* for short) downstream of its native ubiquitously active promoter. Some articles also refer to them as *sqh-mCherry* or *sqh-GFP*. Gifts from Adam Martin (both on chromosome 2).
α-Catenin-YFP is a 'Cambridge Protein Trap Insertion' line (CPTI-002516). DGRC #115551.
67-Gal4 (mat αTub-GAL4-VP16) is ubiquitous, maternally supplied, Gal4 driver.
UAS-ECad::GFP produces GFP-tagged version of wild-type E-cadherin under UAS promoter. For E-cadherin over-expression, virgin females with the genotype '+; 67-Gal4*, MyoII-mCherry, E-cadherin-GFP*; +' or '+; 67-Gal4, *Vinculin-mCherry, E-cadherin-GFP*; +' were crossed to males with genotype +; *UAS-ECad::GFP*; +. Previously used in [43].
UAS-Gα12/13 produces un-tagged version of wild-type Gα12/13, which is the α-subunit of the heterotrimeric G-protein complex. For Gα12/13 overexpression, virgin females with the genotype '+; 67-Gal4, *MyoII-mCherry, E-cadherin-GFP*; +' or '+; 67-Gal4, *Vinculin-mCherry, E-cadherin-GFP*; +' were crossed to males with genotype '+; *UAS-Gα12/13*; +'. Gift from Naoyuki Fuse.
RhoGEF2-RNAi was achieved using RhoGEF2 TRiP line (Bloomington #34643). It produces a short-hairpin RNA downstream of a UAS promoter (*UAS-RhoGEF2-shRNA*) that targets RhoGEF2 mRNA to perform RNAi mediated knock-down. To achieve an effective RNAi during early embryonic development, virgin females with the genotype '+; 67-Gal4*, MyoII-mCherry, E-cadherin-GFP*; +' or '+; 67-Gal4, *Vinculin-mCherry, E-cadherin-GFP*; +' were first crossed to males with genotype '+; +; *UAS-RhoGEF2-shRNA'*. F1 virgins from these crosses were further out-crossed to males with genotype '*y, w*; +; +'.

Embryo preparation, RNAi and drug injections

Embryos were prepared as described before [34,60,61]. Briefly, embryos were dechorionated using bleach, for about 40 seconds and then washed thoroughly with distilled water. The embryos were then aligned on a flat piece of agar and then glued to a glass coverslip. These embryos can be submerged in water and can be imaged directly. Alternatively, glued embryos were kept in an airtight box containing Drierite for about 7 minutes, then covered in halocarbon oil and then injected with either RNase free water itself or RNase free water containing dsRNA or drugs.

α-Catenin RNAi was achieved by injecting dsRNA in embryos (previously used in [9]). dsRNA probes against α-Catenin were made using PCR products containing the sequence of the T7 promoter targeting nucleotides 101–828 of α - Catenin sequence (GenBank accession

D13964). dsRNA prepared as already described were diluted for injection at 5µM concentration and injected within the first hour of embryonic development to achieve maximum knockdown. As a control, separate set of embryos of the same stage were injected with similar volume of RNase free water.

Rok inhibition was achieved through drug injections. H1152 is a membrane permeable pharmacological inhibitor that has high specificity for Rok and blocks its kinase activity. This drug was dissolved in RNase free water @20mM and injected at the end of cellularization. As a control, separate set of embryos of the same stage were injected with similar volume of RNase free water. The reduction in Myosin-II recruitment acts as a direct readout of Rok inhibition. The effect of Rok inhibition on Vinc/E-cad ratio could not be assessed directly, as Myosin-II couldn't be imaged simultaneously. Thus, first the inhibition was performed in embryos expressing MyoII-GFP and Vinculin-mCherry. The reduction in Vinculin intensity can then be used to assess the extent of Rok inhibition in embryos expressing Vinculin-mCherry and E-cadherin-GFP, while also estimating the Vinc/E-cad ratio. The reduction in E-cadherin was cross-checked with another set of embryos expressing E-cadherin-GFP and MyoII-mCherry, where reduction in MyoII-mCherry recruitment acted as a direct readout of Rok inhibition.

Imaging

Time-lapse images were acquired to encompass stage 7 to 8 of the embryonic development [62], which needs ~15min at room temperature (~22^{0}C). Embryos were imaged for 20–30min depending on the experiment, on a Nikon spinning-disk Eclipse Ti inverted microscope using a 100x 1.45 NA oil immersion objective. MyoII-mCherry and E-cadherin-GFP signals were captured every 30s or higher, on 11 Z-planes, separated by 0.5µm. Vinculin-mCherry and E-cadherin-GFP signals were captured every 30s or higher, on 7 Z-planes, separated by 0.5µm. A Nikon spinning-disc Eclipse Ti inverted microscope using a ×100, 1.4 N.A oil immersion objective was used for imaging α-Catenin-YFP. Both systems acquire images using the MetaMorph software. Laser power and exposure settings were optimized to get best signal while minimizing photo-bleaching, and were kept constant between control and perturbation embryos.

Laser ablation experiments

Ablations were performed in a 10-minute time window around stage7b (stage7b ± 5min) on an inverted microscope (Eclipse TE 2000-E, Nikon) equipped with a spinning-disc (Ultraview ERS, Perkin Elmer) for fast imaging. Time lapse at a single z-plane was acquired using a 100x 1.4NA oil immersion objective. Two color images were acquired in sequence on the same camera, when necessary. Ablations were performed in parallel with image acquisition. Ablation events were obtained by exposing the junctions, for duration of 2-3ms, to a near-infrared laser (1,030 nm) focused in a diffraction-limited spot. Laser power at the back aperture of the objective was ~800mW.

Image analysis and Statistics

All image processing was done using FIJI freeware. Raw images were processed using a custom written macro. First, it generated a 'signal image' by using the StackFocuser plug-in to determine the plane of best focus, followed by a maximum-intensity projection of only 3 z-planes (1 z-plane in focus determined by StackFocuser + 2 z-planes basal to it). The macro also

generated a 'background image', first, using a maximum-intensity projection of basal-most 3 planes, followed by applying a 50pixel radius median filter. The macro then subtracted the 'background image' from 'signal image' to produce 'processed image'.

The images were independently segmented using 'Packing analyzer v2.0' (described in [63]), which was implemented as a plugin in FIJI, to get segmented junctional networks. E-Cadherin, Vinculin, Myosin-II or α-Catenin intensities were used, depending on the genotype of the embryos (and in that order of preference), for image segmentation in order to identify cell-cell contacts in a semi-automated manner. Using another custom written macro, the segmentation was used to demarcate the junctional ROIs of about 5 pixel width, such that the vertices (tri-cellular junctions) are excluded. Line densities were measured for the protein of interest to calculate 'mean junctional intensity'. Junctions were categorized based on their angle relative to AP axis into 6 'angle bins' (0-15, 15-30 . . . 75-90 degrees). An average of the junctional line densities was calculated within each 'angle bin' to get 6 values for every embryo. A further average of these 'averaged line densities' acts as a data point per embryo to estimate 'mean junctional intensity' for the protein of interest. The ratio between the 'averaged line density' for '0-15' (AP) and '75-90' (DV) categories produces the 'amplitude of polarity', either AP/DV or DV/AP as mentioned in Y-axis labels. Alternatively, the planar polarity of a protein was represented as 'relative intensity', where the 'averaged line density' values from the 'angle bins' were normalized by the 'average line density' of either '0-15' or '75-90' category, whichever is smaller. In case of Vinc/E-cad ratio, similar calculations were performed after having calculated the ratio between Vinculin and E-cadherin line densities for every junction. The same segmentation was also used to identify the medial ROIs (at least 2 pixels away from any junctional ROI and tri-cellular junctions), for medial Myosin-II intensity estimates. An average of medial area densities was calculated to get one data point per embryo, to estimate 'mean medial intensity' for Myosin-II across multiple embryos.

In case of ablation experiments, images were first processed using the 'rolling ball' background subtraction method implemented in FIJI (rolling ball radius 50). Junctional ROIs were drawn manually (5 pixels wide) on the ablated junction and on 20+ neighboring junctions. Then, the line density of the ablated junction was normalized by the averaged line density of the neighboring junctions. This yielded the 'normalized junctional intensity' for protein of interest. Such normalization is necessary to reduce embryo-to-embryo variability. In case of Vinc/E-cad ratio, similar calculations were performed after having calculated the ratio between Vinculin and E-cadherin line densities for all marked junctions. The vertices of the ablated junction were tracked manually to estimate the recoil velocity in 2 seconds after the ablation. Spearman correlation gave an estimate of the extent of correlation between 'pre-ablation normalized junctional intensity' and corresponding 'post-ablation initial recoil velocity' values.

For 'pixel scale analysis' of Vinc/E-cad ratio, we identified E-cadherin positive pixels by estimating the Signal-to-Noise Ratio (SNR) at all pixels (Supplementary Fig. 6A, B) and measured Vinc/E-cad for the pixels with SNR>1. We empirically decided the range of E-cadherin pixel intensities to span an order of magnitude, such that each intensity range hosts statistically meaningful number of pixels (Supplementary Fig. 6C).

The 'mean values' and 'standard errors on mean' were calculated from 'n' data points. The same data points were used for testing statistical significance. In planar polarity and junctional

intensity measurements, 'n' is the number of embryos. Error bars indicate s.e.m. (i.e., s.d./ √ n). The p-values were estimated using student's t-test, wherever applicable. In laser ablation experiments, 'n' is the number of ablated junctions that are pooled from many embryos. The p-values were estimated using Mann-Whitney U-test. The sample sizes were not predetermined using any statistical methods. The experiments were not randomized, and the investigators were not blinded to allocation during experiments and outcome assessment.

All measurements were performed on 5–25 embryos spread over at least 3 rounds of embryo collections and preparation.

Mechanical Inference

Mechanical inference is an image-based force inference technique that takes a segmented cellular network as the input and estimates relative tensions along cell junctions by assuming force balance at each vertex [48–50,64,65]. We implement mechanical inference on segmented images of cell network based on the E-cadherin channel. We collect 30 images at a time interval of 30 seconds for each embryo. The E-cadherin channel images are processed using the freeware ilastik for pixel classification. The resulting probability maps of pixels are processed using a customized MATLAB script for cell segmentation using a watershed algorithm. The mechanical inference is performed on the segmented image by imposing force balance at each vertex of the cell where junctional tensions add up to zero. We assume a homogeneous pressure distribution across the tissue based on the observation that the junctional curvatures are negligible in the ectoderm during the time window of observation, hence pressure does not enter the force balance equation.

The relative junctional tensions are obtained by fitting a tension triangulation network perpendicular to the corresponding cell network. This is termed the variational mechanical inference as the optimal tension network is obtained by minimizing an energy functional determined by the inner product of the tension network and the cell network [49]. Our analysis has shown that tensions inferred with this method correlate better with Vinc/E-cad ratio or Myosin density as compared to those estimated by a pseudo-inverse of the force balance matrix. The higher accuracy of the variational mechanical inference is due to the global fitting of both the magnitude and the orientation of the tension as opposed to the pseudo-inverse method, which only fits the magnitude of the tension while constraining the direction of the tension along the junctions. The flexibility in the orientation of the tension compensates for the potential errors in the segmentation of the cell, yielding higher accuracy for the mechanical inference. To guarantee the tension network to be a triangulation network, we kept only cells with three-fold vertices, which make up most of the cells in the population. We normalized the average inferred tension to be one. Shear stress on the E-cadherin clusters was obtained from a model of the junction (Fig. 6A) resulting from the transfer of tension from one side of the junction to the other. The shear stress takes the form $\tau=|(T_1+T_3)-(T_2+T_4)|/L$, where 'L' is the length of the junction [48].

Local correlation and conditional correlation

The correlations were performed by binning the junctions according to cell, termed local correlation (Supplementary Figure 2A), or according to junctional length, termed conditional correlation (Supplementary Figure 2A). These two types of correlation are special cases of partial correlation, defined as the correlation between two random variables X and Y while

holding the third variable Z constant, whose correlation coefficient is given by $\rho_{XY|Z} = \frac{1}{\sigma_{X|Z}\sigma_{Y|Z}} E[(X|Z - \mu_{X|Z})(Y|Z - \mu_{Y|Z})]$, where $\sigma_{X|Z}$ ($\sigma_{Y|Z}$) is the standard deviation of X (Y) at fixed Z, and $\mu_{X|Z}$ ($\mu_{Y|Z}$) is the average value of X (Y) at fixed Z. The partial correlation removes the spurious correlation between X and Y due to the confounding variable Z which is related to both X and Y.

The local correlation avoided the temporal and spatial variations of tension and fluorescence intensity, and yielded the correlation coefficient for each cell. We implemented the local correlation by computing the Pearson correlation coefficient between inferred tension and either the Vinc/E-cad ratio, Myosin intensity or Vinculin intensity among junctions within each cell. The resulting correlation coefficients were combined across all cells and multiple embryos to yield a distribution as shown in Figure 2H-J.

The conditional correlation avoided the spurious intensity-intensity and intensity-tension correlation resulting from the variation of junctional length, because both the intensities and the inferred tension are proportional to the inverse of junctional length (Supplementary Fig. 4A). It also yielded the correlation coefficient as a function of junctional length (Figure 6D and F, Supplementary Fig. 2C and 4C). We implemented the conditional correlation by sorting 10 junctions of the same length into the same bin. A linear correlation coefficient was computed among these 10 junctions with the same length for Vinculin and E-cadherin intensity (Supplementary Fig. 2C), E-cadherin intensity and inferred shear (Fig. 6D and F), junctional intensity and inferred tension (Supplementary Fig. 4C). The binning was performed independently for each snapshot to avoid temporal and inter-embryo variations. Finally, we obtained the distribution of the conditional correlation coefficient by combining all the bins across time points and embryos (Fig. 6C and E, Supplementary Fig. 2B and 4B).

Figure legends

Figure1: Regulation of Vinculin localization

(A-C'') Vinculin is recruited to E-cadherin based adhesion complexes and this recruitment requires α-Catenin. (A) Colocalization between E-cadherin and Vinculin. Various E-cadherin clusters (arrowheads) colocalize with those of Vinculin. (B) Top panels, zoom-in view of boxed junction in 'A'. Bottom panel shows the similarities in the intensity profiles for Vinculin and E-cadherin. (C) Representative images showing the distribution of Vinculin in water-injected embryo (left) and α-Catenin dsRNA injected embryo (right). (C', C'') Quantifications showing a reduction in Vinculin recruitment and a loss of the planar polarized distribution of Vinculin due to α-Catenin RNAi. Number of embryos in inset.

(D-G'') Vinculin enrichment relative to E-cadherin is tuned by Myosin-II activity. Rok inhibitor H1152 was injected @ 20mM concentration to inhibit Myosin-II activity. (D, E, F and G) Representative images showing the distribution of Myosin-II, Vinculin, E-cadherin and Vinc/E-cad ratio, respectively, in water-injected control embryos (left panels) and H1152-injected embryos (right panels). (D', D'') Quantifications showing a reduction in junctional Myosin-II recruitment and a loss of its planar polarized distribution due to Rok inhibition. Number of embryos in inset. (E', E'') Quantifications showing a reduction in Vinculin recruitment and an inversion of its planar polarized distribution due to Rok inhibition. Number of embryos in inset.

(F', F'') Quantifications showing the reduction in E-cadherin levels and an amplification of its planar polarized distribution due to Rok inhibition. Number of embryos in inset. Corresponding representative images and quantifications for changes in Myosin-II distribution are presented in Figure 4A-A''. (G', G'') Quantifications showing a reduction in Vinc/E-cad ratio and a loss of its planar polarized distribution due to Rok inhibition. Number of embryos in inset.

All scale bars represent 5µm. Statistical significance estimated using 'Student's t-test'. Images/quantifications in A-C'' and G-G'' come from embryos co-expressing Vinculin-mCherry and E-cadherin-GFP. Junctions marked based on E-cadherin localization. Images/quantifications in D-E'' come from embryos co-expressing Vinculin-mCherry and MyoII-GFP. Junctions marked based on Vinculin localization. Images/quantifications in F-F'' come from embryos co-expressing MyoII-mCherry and E-cadherin-GFP. Junctions marked based on E-cadherin localization.
ns, $p>0.05$; *, $p<0.05$; **, $p<0.01$; ***, $p<0.001$; ****, $p<0.0001$

Figure2: Vinc/E-cad ratio correlates with the junctional tension
(A-C) Vinc/E-cad ratio correlates with junctional tension estimated in laser ablation experiments. (A) Schematic representation of junctional recoil after an event of ablation. Junctions under low tension (top panels) show slower initial recoil, whereas junctions under high tension (bottom panels) show faster initial recoil. (B, C) A scatter plot showing the distribution of the pre-ablation (B) junctional Myosin-II intensities or (C) Vinc/E-cad ratio against the post-ablation recoil velocities for multiple events of junctional ablations. In insets, Spearman correlation coefficient 'ρ' with corresponding 'p-value', and number of ablations events 'n' pooled from 'N' embryos.
(D-G) Vinc/E-cad ratio correlates with junctional tension estimated using mechanical inference. (D, E) Representative images showing the distribution of Vinc/E-cad ratio (yellow colors indicate higher ratio) and corresponding distribution of inferred tension (thicker lines indicate higher tension). (F, G) The distributions of Vinc/E-cad ratio and inferred tension show similar planar polarity. Number of embryos in inset.
(H-J) Vinc/E-cad ratio and Myosin-II have similar extent of local correlation with inferred tension. Box plots showing the distribution of local correlation coefficients between the inferred tension and either the Junctional Myosin-II (H, n=3500 cells), the Vinc/E-cad ratio (I, n=9000 cells) or the Vinculin intensity (J, n=9000 cells), for WT embryos, H1152 injected embryos along with statistical null.

Quantifications in B and C come respectively from embryos expressing MyoII-GFP or embryos co-expressing Vinculin-mCherry and E-cadherin-GFP. Images/Quantifications in D-G come from embryos co-expressing Vinculin-mCherry and E-cadherin-GFP. Inferred tension junctional Myosin-II correlations were estimated in appropriately injected embryos co-expressing MyoII-mCherry and E-cadherin-GFP (data in H). Inferred tension Vinc/E-cad ratio correlations were estimated in appropriately injected embryos co-expressing Vinculin-mCherry and E-cadherin-GFP (data in I and J). The boxes in H, I and J represent 25^{th}percentiles to 75^{th}percentiles; the whiskers represent 5^{th}percentiles to 95^{th}percentiles; and the red lines represent the medians.

Figure3: Vinc/E-cad ratio represents the load on adhesion complexes.
Mild over-expression of E-cadherin reduces Vinc/E-cad ratio levels without changes in either the distribution of Myosin-II or the tension on junctions.

(A) Schematics showing the effect of E-cadherin over-expression on Vinculin recruitment. In the WT scenario, Vinculin recruitment is driven by the amount of tension generated by actomyosin contractility loaded on each adhesion complex. After E-cadherin overexpression, the same tension is supported by more adhesion complexes, leading to less Vinculin recruitment, which would result in an overall decrease of Vinc/E-cad ratio.
(B, C, D, E) Representative images showing the distribution of E-cadherin, Vinculin, Vinc/E-cad ratio and Myosin-II, respectively, in genetic outcross control embryos (left panels) and E-cadherin over-expressing embryos (right panels). (B') Quantifications showing an increase in E-cadherin levels at the junctions, quantified as increase in mean junctional intensity. (C') Quantifications showing a decrease in Vinculin levels at the junctions, quantified as a decrease in mean junctional intensity. (D') Quantifications showing a reduction in mean junctional Vinc/E-cad ratio. (E' and E'') Quantifications showing that the distribution of Myosin-II hasn't changed upon E-cadherin over-expression.
(F) Quantifications showing Vinc/E-cad ratio estimated at the scale of individual pixels and plotted against corresponding E-cadherin pixel bin intensity. Each bin is 25 intensity units wide. The Vinc/E-cad ratio represents the average of Vinc/E-cad ratio for all pixels in that bin, separately estimated for individual embryos. Mean and SEM are calculated across embryos.

All scale bars represent 5µm. Statistical significances were estimated using 'Student's t-test'. For the data in B', C', D', E', E'' and F n=7 embryos for both, control and UAS-E-cad::GFP. Images/quantifications in B, B' and E-E'' come from embryo co-expressing MyoII-mCherry and E-cadherin-GFP. Images/quantifications in C-D' and F come from embryo co-expressing Vinculin-mCherry and E-cadherin-GFP. In all cases, Junctions/pixels marked based on E-cadherin localization.
ns, $p>0.05$; *, $p<0.05$; **, $p<0.01$; ***, $p<0.001$

Figure4: Medial Myosin tunes the levels of Vinc/E-cad ratio, while junctional Myosin tunes its planar polarized distribution
<u>Inhibition of Myosin-II activity reduces the levels of Vinc/E-cad ratio and abolishes its planar polarity.</u> (A, B) Representative images showing the distribution of Myosin-II and Vinc/E-cad ratio, respectively, in the water injection 'control' embryos (left) and H1152 injected 'Rok inhibition' embryos (right). (A' and A'') Quantifications showing the reduction in the levels of Myosin-II in the medial and junction pool, along with a loss of planar polarity, upon Rok inhibition. Data from n=7 embryos for both controls and Rok inhibitions. (B') Quantifications showing a reduction in mean junctional Vinc/E-cad ratio, along with a loss of polarity. Data from n=6 embryos for controls and n=7 for Rok inhibitions.
<u>Inhibition of Myosin-II activity in the medial pool using RhoGEF2-RNAi, reduces the levels Vinc/E-cad ratio, without affecting its planar polarized distribution.</u> (C, D) Representative images showing the distribution of Myosin-II and Vinc/E-cad ratio, respectively, in the genetic outcross control embryos (left) and RhoGEF2-RNAi embryos (right). (C' and C'') Quantifications showing the reduction in the levels of medial Myosin-II, without a change in the distribution of junctional Myosin-II. Data from n=8 embryos for both RhoGEF2-RNAi and control. (D') Quantifications showing a reduction in mean junctional Vinc/E-cad ratio, without an effect on its planar polarized distribution. Data from n=6 embryos for control and n=7 embryos for RhoGEF2-RNAi.
<u>Hyper-activation of Myosin-II in the medial pool using Gα12/13 over-expression, increases the levels Vinc/E-cad ratio, without affecting its planar polarized distribution.</u> (E, F) Representative

images showing the distribution of Myosin-II and Vinc/E-cad ratio, respectively, in the genetic outcross control embryos (left) and Gα12/13 over-expressing embryos (right). (E' and E'') Quantifications showing the increase in the levels of medial Myosin-II, without a significant change in the distribution of junctional Myosin-II. Data from n=7 embryos for both Gα12/13 over-expression and control. (D') Quantifications showing an increase in the mean junctional Vinc/E-cad ratio, without a significant effect on its planar polarized distribution. Data from n=7 embryos for control and n=6 embryos for Gα12/13 over-expression.

All scale bars represent 5µm. Statistical significance estimated using 'Student's t-test'. Images/quantifications in A-A'', C-C'' and E-E'' come from embryo co-expressing MyoII-mCherry and E-cadherin-GFP. Images/ quantifications in B-B', D-D' and F-F' come from embryo co-expressing Vinculin-mCherry and E-cadherin-GFP. In all cases, Junctions marked based on E-cadherin localization. Images/quantifications in B-B' are from the same set of embryos as those presented in Figure 1G-G''.
ns, $p>0.05$; *, $p<0.05$; **, $p<0.01$; ***, $p<0.001$; ****, $p<0.0001$

Figure5: Medial Myosin-II tunes the levels of junctional E-cadherin
<u>A reduction (increase) in medial Myosin-II correlates with a decrease (increase) in the global junctional levels of E-cadherin.</u>
(A) Representative images showing the distribution of E-cadherin, in the genetic outcross control embryos (left) and RhoGEF2-RNAi embryos (right). (A') Quantifications showing the reduction in E-cadherin levels, quantified as mean junctional intensity. Data from n=8 embryos for both RhoGEF2-RNAi and control.
(B) Representative images showing the distribution of E-cadherin, in the genetic outcross control embryos (left) and Gα12/13 over-expressing embryos (right). (B') Quantifications showing an increase in E-cadherin levels, quantified as mean junctional intensity. Data from n=7 embryos for both Gα12/13 over-expression and control.

All scale bars represent 5µm. Statistical significance estimated using 'Student's t-test'. Images/quantifications in all panels come from embryo co-expressing MyoII-mCherry and E-cadherin-GFP. In all cases, Junctions marked based on E-cadherin localization.
ns, $p>0.05$; *, $p<0.05$; **, $p<0.01$; ***, $p<0.001$

Figure6: Shear stress is negatively correlated with the levels of junctional E-cadherin
(A) Schematic representation of a model of the junction to construct shear and the corresponding equation of shear stress. Blue lines denote junctional Myosin-II, green lines denote E-cadherin, and yellow arrows denote the inferred tension on junction.
(B) Correlation of inferred tension and shear with E-cadherin intensity conditioned on the length of the junction. The statistics are based on 19500 junctions across 5 embryos with 10 junctions in one conditional bin.
(C, D) Correlation of inferred tension and shear with E-cadherin intensity conditioned on the length of the junction, only for the vertical junctions from a subset of the data in B.
(E, F) Correlation of inferred shear with E-cadherin intensity conditioned on the length of the junction for vertical and transverse junctions for wild-type and Rok inhibited embryos. The statistics for wild-type (Rok inhibited) embryos are based on 15000 junctions across 5 (10) embryos with 10 junctions in one conditional bin for both transverse and vertical junctions.

The error bars in D and F represent the standard error across 100 different bins with the same length of junction. The boxes in B, C and E represent 25thpercentiles to 75thpercentiles; the whiskers represent 5thpercentiles to 95thpercentiles; and the red lines represent the medians.

Supplementary Figure1: Vinculin distribution in the embryonic ectoderm
Apico-basal polarity: (A) Schematic representation of apical region of the ectodermal cells. Various horizontal lines correspond to cross-sections shown in B, C and D. (B-D) Planar view of E-cadherin, Myosin-II and Vinculin at different z-steps of 1µm from apical surface. E-cadherin, Myosin-II and Vinculin enrichment in junctional plane is evident.
Planar polarity: (E-H) Images showing z-projection over 3µm apical region to represent junctional localization of E-cadherin, α-Catenin, Myosin-II and Vinculin, respectively. Boundary between cytoplasm and cell contacts is emphasized in G, as Myosin-II distribution doesn't mark all junctions. (E'-H') Quantifications for planar polarity averaged across multiple embryos (n=5, 7, 6 and 7 embryos for E-cadherin, α-Catenin, Myosin-II and Vinculin, respectively). Error bars represent SEM.

All scale bars are 5µm. Images/quantifications in B, E and E' come from embryos expressing E-cadherin-GFP. Images/quantifications in C, G and G' come from embryos expressing MyoII-GFP. Images/quantifications in D, H and H' come from embryos expressing Vinculin-GFP. Images/quantifications in F and F' come from embryos expressing α-Catenin-YFP.

Supplementary Figure2: Correlations analysis and Vinculin- E-cadherin conditional correlation
(A) Schematic representation to describe 'conditional correlation' and 'local correlation'. Various junctions are numbered as shown. Similarly colored junctions belong to the same length category and will be binned together for 'conditional correlation' analysis. Junctions of the same cell will be binned together for 'local correlation' analysis. Also, see Methods.
(B, C) Conditional correlation of Vinculin intensity with E-cadherin intensity conditioned on the length of the junction for wild-type and Rok inhibited embryos. The statistics are based on 35180 junctions across 6 embryos with 10 junctions in one conditional bin for both wild-type and Rok inhibited embryos.

The boxes in B represent 25thpercentiles to 75thpercentiles; the whiskers represent 5thpercentiles to 95thpercentiles; and the red lines represent the medians. The error bars in C represent the standard error across 100 different bins with the same length of junction. Vinculin- E-cadherin correlations in B and C were estimated for appropriately injected embryos co-expressing Vinculin-mCherry and E-cadherin-GFP.

Supplementary Figure3: Ablation analyses for Vinculin and E-cadherin densities
(A, B) A scatter plot showing the distribution of the pre-ablation quantities plotted against the post-ablation recoil velocities for n=76 events of junctional ablation, pooled from 25 embryos. (A) Junctional Vinculin intensity, (B) junctional E-cadherin intensity. Junctional intensities on ablated junctions are normalized by the junctional intensities on their neighboring junctions to reduce embryo-to-embryo variation. Spearman correlation coefficient 'ρ' and corresponding p-value in inset. Quantifications in both A and B come from embryos co-

expressing Vinculin-mCherry and E-cadherin-GFP. This data set corresponds to the same ablation events as those in Figure 2C.

Supplementary Figure4: Correlations with inferred tension
(A) Box plots showing the distribution of correlation coefficient between inferred tension and the inverse of junction length based on local correlation. The statistics are based on 9000 cells across 6 embryos.
(B, C) Correlation of Vinc/E-cad ratio, Vinculin and junctional Myosin-II intensity with inferred tension conditioned on the length of the junction. Vinc/E-cad ratio displays the strongest correlation with inferred tension. The statistics are based on 37350 junctions across 6 embryos with 10 junctions in one conditional bin.

The boxes in A and B represent 25thpercentiles to 75thpercentiles; the whiskers represent 5thpercentiles to 95thpercentiles; and the red lines represent the medians. The error bars in 'C' represent the standard error across 100 different bins with the same length of junction. Inferred tension- Vinculin and inferred tension- Vinc/E-cad ratio correlations in B and C were estimated for embryos co-expressing Vinculin-mCherry and E-cadherin-GFP. Inferred tension-Myosin-II correlations in B and C were estimated for embryos co-expressing MyoII-mCherry and E-cadherin-GFP.

Supplementary Figure5: Ablation analyses to estimate the distribution of junctional tension
(A) The distribution of recoil velocities didn't change in either the transverse or vertical junctions upon E-cadherin over-expression, indicating that the distribution of junctional tension hasn't changed either. Number of ablated junctions in each category is indicated next to its distribution. Transverse and vertical junctions pooled from various ablation events in 17 embryos for control and 9 embryos for UAS-E-cad::GFP
(B) The recoils are faster upon RhoGEF2-RNAi, in both the transverse and vertical junctions, indicating that the junctional tension hasn't decreased. Number of ablated junctions in each category is indicated next to its distribution. Transverse and vertical junctions pooled from various ablation events in 14 embryos for control and 9 embryos for RhoGEF2-RNAi.

Statistical significance estimated using 'Mann-Whitney U-test'. Quantifications in 'A' come from embryos co-expressing MyoII-mCherry and E-cadherin-GFP, with or without accompanying E-cadherin over-expression. Quantifications in 'B' come from embryos expressing MyoII-GFP, with or without accompanying RhoGEF2-RNAi.
ns, $p>0.05$

Supplementary Figure6: Supporting information for 'pixel analysis' of Vinc/E-cad ratio
(A) Schematic representation of the concept employed to identify pixels positive for E-cadherin. Signal-to-Noise Ratio (SNR) provides a completely objective way to determine a signal pixel. SNR is estimated using a simple local estimation of the ratio between the mean (μ) of pixel intensities and the standard deviation (σ) of pixel intensities. At the signal pixel, the ratio of pixel intensities from Vinculin and E-cadherin image channels gives the Vinc/E-cad ratio.
(B) Representative images showing the conversion from E-cadherin channel image to SNR image. The E-cadherin-GFP images are at 1, 2 or 3µm distance from the surface of the embryo

(similar to Supplementary Fig. 1B). The corresponding SNR images show all pixels with intensity>1. In such a representation, all cytoplasmic pixels are blank. Scale bar 5µm.
(C) Quantifications showing the number of pixels in various E-cadherin pixel intensity bins. Each bin is 25 intensity units wide. The number of pixels is comparable between control and E-cadherin over-expressing embryos, across an order of a magnitude of pixel intensities. Number of pixels in a bin are separately estimated for individual embryos. Mean and SEM are calculated across embryos. Arrow indicates the minimum average number of pixels required to have meaningful statistics for individual embryos in both control and E-cadherin over-expressing embryos.

References

1. Lecuit, T., Lenne, P.-F. & Munro, E. Force generation, transmission, and integration during cell and tissue morphogenesis. *Annu. Rev. Cell Dev. Biol.* **27,** 157–84 (2011).
2. Heisenberg, C.-P. & Bellaïche, Y. Forces in Tissue Morphogenesis and Patterning. *Cell* **153,** 948–962 (2013).
3. Hunter, M. V & Fernandez-Gonzalez, R. Coordinating cell movements in vivo : junctional and cytoskeletal dynamics lead the way. *Curr. Opin. Cell Biol.* **48,** 54–62 (2017).
4. Yap, A. S., Duszyc, K. & Viasnoff, V. Mechanosensing and Mechanotransduction at Cell–Cell Junctions. *Cold Spring Harb. Perspect. Biol.* a028761 (2017). doi:10.1101/cshperspect.a028761
5. Truong Quang, B. A., Mani, M., Markova, O., Lecuit, T. & Lenne, P. F. Principles of E-cadherin supramolecular organization in vivo. *Curr. Biol.* **23,** 2197–2207 (2013).
6. Wu, Y., Kanchanawong, P. & Zaidel-Bar, R. Actin-Delimited Adhesion-Independent Clustering of E-Cadherin Forms the Nanoscale Building Blocks of Adherens Junctions. *Dev. Cell* **32,** 139–154 (2015).
7. Yap, A. S., Gomez, G. A. & Parton, R. G. Adherens Junctions Revisualized: Organizing Cadherins as Nanoassemblies. *Dev. Cell* **35,** 12–20 (2015).
8. Sako, Y., Nagafuchi, A., Tsukita, S., Takeichi, M. & Kusumi, A. Cytoplasmic regulation of the movement of E-cadherin on the free cell surface as studied by optical tweezers and single particle tracking: corralling and tethering by the membrane skeleton. *J. Cell Biol.* **140,** 1227–40 (1998).
9. Cavey, M., Rauzi, M., Lenne, P.-F. & Lecuit, T. A two-tiered mechanism for stabilization and immobilization of E-cadherin. *Nature* **453,** 751–6 (2008).
10. Yonemura, S., Wada, Y., Watanabe, T., Nagafuchi, A. & Shibata, M. alpha-Catenin as a tension transducer that induces adherens junction development. *Nat. Cell Biol.* **12,** 533–42 (2010).
11. Buckley, C. D. *et al.* Cell adhesion. The minimal cadherin-catenin complex binds to actin filaments under force. *Science* **346,** 1254211 (2014).
12. le Duc, Q. *et al.* Vinculin potentiates E-cadherin mechanosensing and is recruited to actin-anchored sites within adherens junctions in a myosin II-dependent manner. *J. Cell Biol.* **189,** 1107–1115 (2010).
13. Engl, W., Arasi, B., Yap, L. L., Thiery, J. P. & Viasnoff, V. Actin dynamics modulate mechanosensitive immobilization of E-cadherin at adherens junctions. *Nat. Cell Biol.* **16,** 587–94 (2014).
14. Adams, C. L., Chen, Y. T., Smith, S. J. & Nelson, W. J. Mechanisms of epithelial cell-cell adhesion and cell compaction revealed by high-resolution tracking of E-cadherin-green fluorescent protein. *J. Cell Biol.* **142,** 1105–19 (1998).
15. Chu, Y.-S. *et al.* Force measurements in E-cadherin-mediated cell doublets reveal rapid adhesion strengthened by actin cytoskeleton remodeling through Rac and Cdc42. *J. Cell Biol.* **167,** 1183–94 (2004).
16. Maître, J.-L. *et al.* Adhesion Functions in Cell Sorting by Mechanically Coupling the Cortices of Adhering Cells. *Science* **338,** 253–6 (2012).
17. Rangarajan, E. S. & Izard, T. The cytoskeletal protein α-catenin unfurls upon binding to vinculin. *J. Biol. Chem.* **287,** 18492–9 (2012).
18. Kim, T. J. *et al.* Dynamic visualization of α-catenin reveals rapid, reversible

conformation switching between tension states. *Curr. Biol.* **25,** 218–224 (2015).
19. Thomas, W. A. *et al.* alpha-Catenin and vinculin cooperate to promote high E-cadherin-based adhesion strength. *J. Biol. Chem.* **288,** 4957–4969 (2013).
20. Barry, A. K. *et al.* α-Catenin cytomechanics: role in cadherin-dependent adhesion and mechanotransduction. *J. Cell Sci.* 1779–1791 (2014). doi:10.1242/jcs.139014
21. Nelson, W. J. & Weis, W. I. 25 Years of Tension over Actin Binding to the Cadherin Cell Adhesion Complex: The Devil is in the Details. *Trends Cell Biol.* **26,** 471–473 (2016).
22. Mège, R. M. & Ishiyama, N. Integration of Cadherin Adhesion and Cytoskeleton at *Adherens* Junctions. *Cold Spring Harb. Perspect. Biol.* a028738 (2017). doi:10.1101/cshperspect.a028738
23. Coopman, P. & Djiane, A. Adherens Junction and E-Cadherin complex regulation by epithelial polarity. *Cell. Mol. Life Sci.* **73,** 3535–3553 (2016).
24. Ladoux, B., Nelson, W. J., Yan, J. & Mège, R. M. The mechanotransduction machinery at work at adherens junctions. *Integr. Biol.* **7,** 1109–1119 (2015).
25. Lecuit, T. & Yap, A. S. E-cadherin junctions as active mechanical integrators in tissue dynamics. *Nat. Cell Biol.* **17,** 533–539 (2015).
26. West, J. J. & Harris, T. J. C. Cadherin Trafficking for Tissue Morphogenesis: Control and Consequences. *Traffic* **17,** 1233–1243 (2016).
27. Hoffman, B. D. & Yap, A. S. Towards a Dynamic Understanding of Cadherin-Based Mechanobiology. *Trends Cell Biol.* **25,** 803–814 (2015).
28. Avizienyte, E., Fincham, V. J., Brunton, V. G. & Frame, M. C. Src SH3/2 domain-mediated peripheral accumulation of Src and phospho-myosin is linked to deregulation of E-cadherin and the epithelial-mesenchymal transition. *Mol. Biol. Cell* **15,** 2794–803 (2004).
29. de Beco, S., Perney, J. B., Coscoy, S. & Amblard, F. Mechanosensitive adaptation of E-cadherin turnover across adherens junctions. *PLoS One* **10,** 1–14 (2015).
30. de Beco, S., Gueudry, C., Amblard, F. & Coscoy, S. Endocytosis is required for E-cadherin redistribution at mature adherens junctions. *Proc. Natl. Acad. Sci. U. S. A.* **106,** 7010–5 (2009).
31. Jurado, J., de Navascués, J. & Gorfinkiel, N. α-Catenin stabilises Cadherin-Catenin complexes and modulates actomyosin dynamics to allow pulsatile apical contraction. *J. Cell Sci.* **129,** 4496–4508 (2016).
32. Weng, M. & Wieschaus, E. Myosin-dependent remodeling of adherens junctions protects junctions from Snail-dependent disassembly. *J. Cell Biol.* **212,** 219–229 (2016).
33. Irvine, K. D. & Wieschaus, E. Cell intercalation during Drosophila germband extension and its regulation by pair-rule segmentation genes. *Development* **120,** 827–41 (1994).
34. Bertet, C., Sulak, L. & Lecuit, T. Myosin-dependent junction remodelling controls planar cell intercalation and axis elongation. *Nature* **429,** 667–671 (2004).
35. Blankenship, J. T., Backovic, S. T., Sanny, J. S. P., Weitz, O. & Zallen, J. a. Multicellular rosette formation links planar cell polarity to tissue morphogenesis. *Dev. Cell* **11,** 459–70 (2006).
36. Collinet, C., Rauzi, M., Lenne, P. & Lecuit, T. Local and tissue-scale forces drive oriented junction growth during tissue extension. *Nat. Cell Biol.* **17,** 1247–58 (2015).
37. Rauzi, M., Lenne, P.-F. & Lecuit, T. Planar polarized actomyosin contractile flows control epithelial junction remodelling. *Nature* **468,** 1110–1114 (2010).
38. Kerridge, S. *et al.* Modular activation of Rho1 by GPCR signalling imparts polarized myosin II activation during morphogenesis. *Nat. Cell Biol.* **18,** 261–270 (2016).

39. Rauzi, M., Verant, P., Lecuit, T. & Lenne, P.-F. Nature and anisotropy of cortical forces orienting Drosophila tissue morphogenesis. *Nat. Cell Biol.* **10,** 1401–10 (2008).
40. Bambardekar, K., Clément, R., Blanc, O., Chardès, C. & Lenne, P.-F. Direct laser manipulation reveals the mechanics of cell contacts in vivo. *Proc. Natl. Acad. Sci.* **112,** 1416–1421 (2015).
41. Zallen, J. a & Wieschaus, E. Patterned gene expression directs bipolar planar polarity in Drosophila. *Dev. Cell* **6,** 343–55 (2004).
42. Simões, S. de M., Mainieri, A. & Zallen, J. A. Rho GTPase and Shroom direct planar polarized actomyosin contractility during convergent extension. *J. Cell Biol.* **204,** 575–89 (2014).
43. Levayer, R. & Lecuit, T. Oscillation and Polarity of E-Cadherin Asymmetries Control Actomyosin Flow Patterns during Morphogenesis. *Dev. Cell* **26,** 162–175 (2013).
44. Hara, Y., Shagirov, M. & Toyama, Y. Cell Boundary Elongation by Non-autonomous Contractility in Cell Oscillation. *Curr. Biol.* **26,** 2388–2396 (2016).
45. Farhadifar, R., Röper, J.-C., Aigouy, B., Eaton, S. & Jülicher, F. The Influence of Cell Mechanics, Cell-Cell Interactions, and Proliferation on Epithelial Packing. *Curr. Biol.* **17,** 2095–2104 (2007).
46. Fernandez-Gonzalez, R., Simoes, S. D. M., Röper, J.-C., Eaton, S. & Zallen, J. a. Myosin II dynamics are regulated by tension in intercalating cells. *Dev. Cell* **17,** 736–43 (2009).
47. Fernandez-Gonzalez, R. & Zallen, J. a. Oscillatory behaviors and hierarchical assembly of contractile structures in intercalating cells. *Phys. Biol.* **8,** 45005 (2011).
48. Chiou, K. K., Hufnagel, L. & Shraiman, B. I. Mechanical stress inference for two dimensional cell arrays. *PLoS Comput. Biol.* **8,** e1002512 (2012).
49. Noll, N., Mani, M., Heemskerk, I., Streichan, S. J. & Shraiman, B. I. Active tension network model suggests an exotic mechanical state realized in epithelial tissues. *Nat. Phys.* (2017). doi:10.1038/nphys4219
50. Yang, X. *et al.* Correlating cell shape and cellular stress in motile confluent tissues. *Proc. Natl. Acad. Sci. U. S. A.* **114,** 12663–12668 (2017).
51. Yao, M. *et al.* Force-dependent conformational switch of α-catenin controls vinculin binding. *Nat. Commun.* **5,** (2014).
52. Munjal, A., Philippe, J.-M., Munro, E. & Lecuit, T. A self-organized biomechanical network drives shape changes during tissue morphogenesis. *Nature* **524,** 351–355 (2015).
53. Biswas, K. H., Hartman, K. L., Zaidel-Bar, R. & Groves, J. T. Sustained α-catenin Activation at E-cadherin Junctions in the Absence of Mechanical Force. *Biophys. J.* **111,** 1044–52 (2016).
54. Braga, V. M. M., Machesky, L. M., Hall, A. & Hotchin, N. a. The small GTPases Rho and Rac are required for the establishment of cadherin-dependent cell-cell contacts. *J. Cell Biol.* **137,** 1421–31 (1997).
55. Carramusa, L., Ballestrem, C., Zilberman, Y. & Bershadsky, A. D. Mammalian diaphanous-related formin Dia1 controls the organization of E-cadherin-mediated cell-cell junctions. *J. Cell Sci.* **120,** 3870–3882 (2007).
56. Priya, R. *et al.* Feedback regulation through myosin II confers robustness on RhoA signalling at E-cadherin junctions. *Nat. Cell Biol.* **17,** 1282–1293 (2015).
57. Alatortsev, V. E., Kramerova, I. A., Frolov, M. V., Lavrov, S. A. & Westphal, E. D. Vinculin gene is non-essential in Drosophila melanogaster. *FEBS Lett.* **413,** 197–201 (1997).
58. Ejsmont, R. K., Sarov, M., Winkler, S., Lipinski, K. A. & Tomancak, P. A toolkit for high-

throughput, cross-species gene engineering in Drosophila. *Nat. Methods* **6,** 435–437 (2009).
59. Huang, J., Zhou, W., Dong, W., Watson, A. M. & Hong, Y. Directed, efficient, and versatile modifications of the Drosophila genome by genomic engineering. *Proc. Natl. Acad. Sci.* **106,** 8284–8289 (2009).
60. Pilot, F., Philippe, J.-M., Lemmers, C., Chauvin, J.-P. & Lecuit, T. Developmental control of nuclear morphogenesis and anchoring by charleston, identified in a functional genomic screen of Drosophila cellularisation. *Development* **133,** 711–23 (2006).
61. Cavey, M. & Lecuit, T. Imaging cellular and molecular dynamics in live embryos using fluorescent proteins. *Methods Mol. Biol.* **420,** 219–38 (2008).
62. Campos-Ortega, J. A. & Hartenstein, V. *The Embryonic Development of Drosophila melanogaster*. **86,** (Springer Berlin Heidelberg, 1985).
63. Aigouy, B. *et al.* Cell Flow Reorients the Axis of Planar Polarity in the Wing Epithelium of Drosophila. *Cell* **142,** 773–786 (2010).
64. Brodland, G. W. *et al.* Video force microscopy reveals the mechanics of ventral furrow invagination in Drosophila. *Proc. Natl. Acad. Sci. U. S. A.* **107,** 22111–6 (2010).
65. Ishihara, S. & Sugimura, K. Bayesian inference of force dynamics during morphogenesis. *J. Theor. Biol.* **313,** 201–11 (2012).

Acknowledgements

We thank members of Lecuit and Lenne group for discussions throughout the course of this project and for providing a stimulating environment, Claire Chardes (Lenne group) and Claudio Collinet (Lecuit group) for assistance with laser ablation experiments, IBDM imaging facility for assistance with maintenance of the Microscopes, FlyBase for maintaining curated database and Bloomington fly facility for providing transgenenic flies.
GK was supported by PhD fellowship from the LabEx INFORM (ANR-11-LABX-0054) and of the A*MIDEX project (ANR-11-IDEX-0001–02), funded by the 'Investissements d'Avenir French Government program'. We thank Satyajit Mayor for arranging a Bridging Post-doctoral fellowship to further support G.K. at NCBS, Bangalore, India. We acknowledge France-BioImaging infra-structure supported by the French National Research Agency (ANR–10–INSB-04-01, «Investments for the future»).

Author contributions

G.K., X.Y., M.M., PF.L. and T.L planned the project. G.K. did the experiments, X.Y. performed the mechanical inference studies, JMP. did the constructs. G.K. and X.Y. did the analysis. All authors discussed the data. G.K, X.Y. and T.L. wrote the manuscript and all authors gave comments on the manuscript.

Figure1: Regulation of Vinculin localization

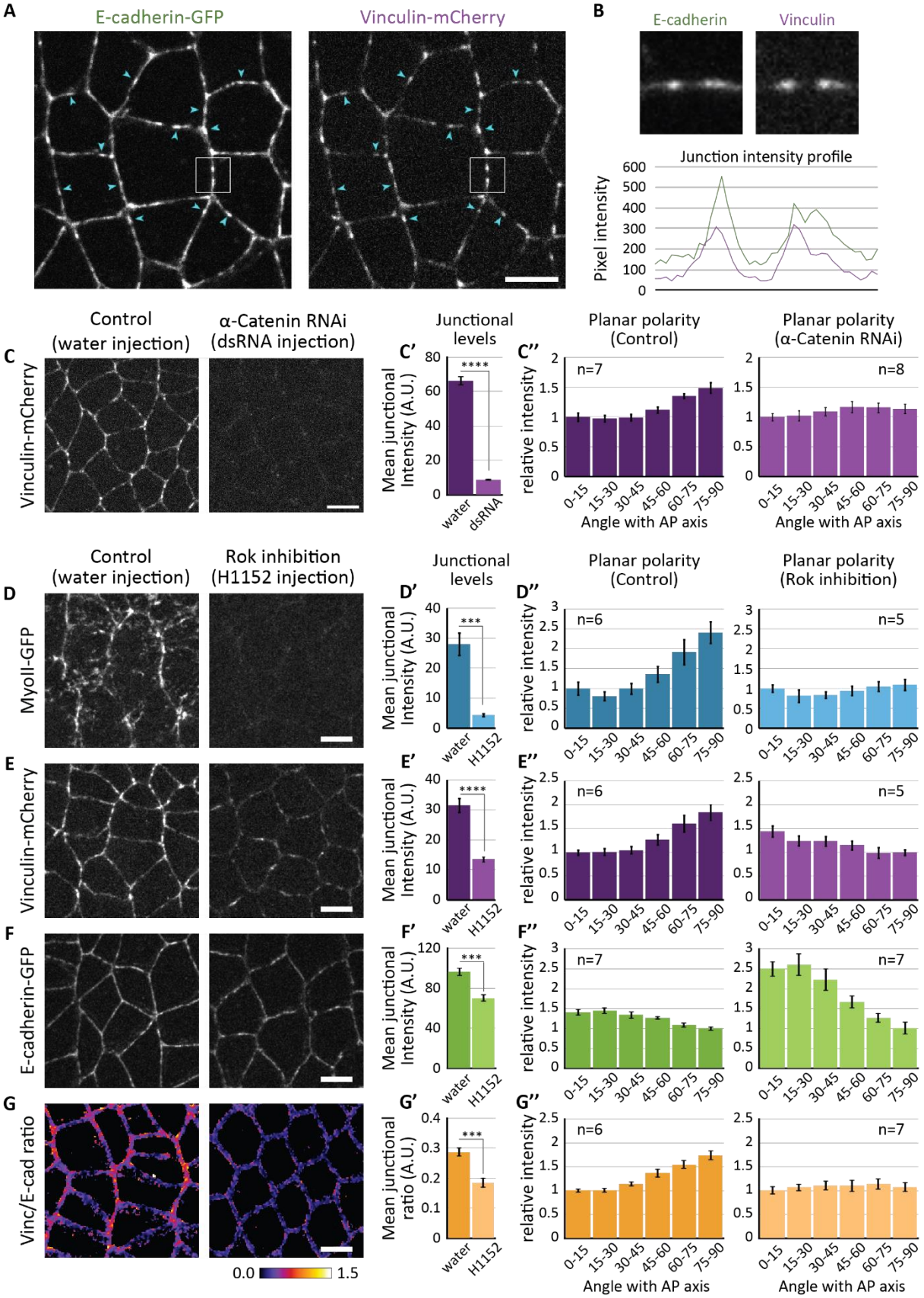

Figure2: Vinc/E-cad ratio correlates with the junctional tension

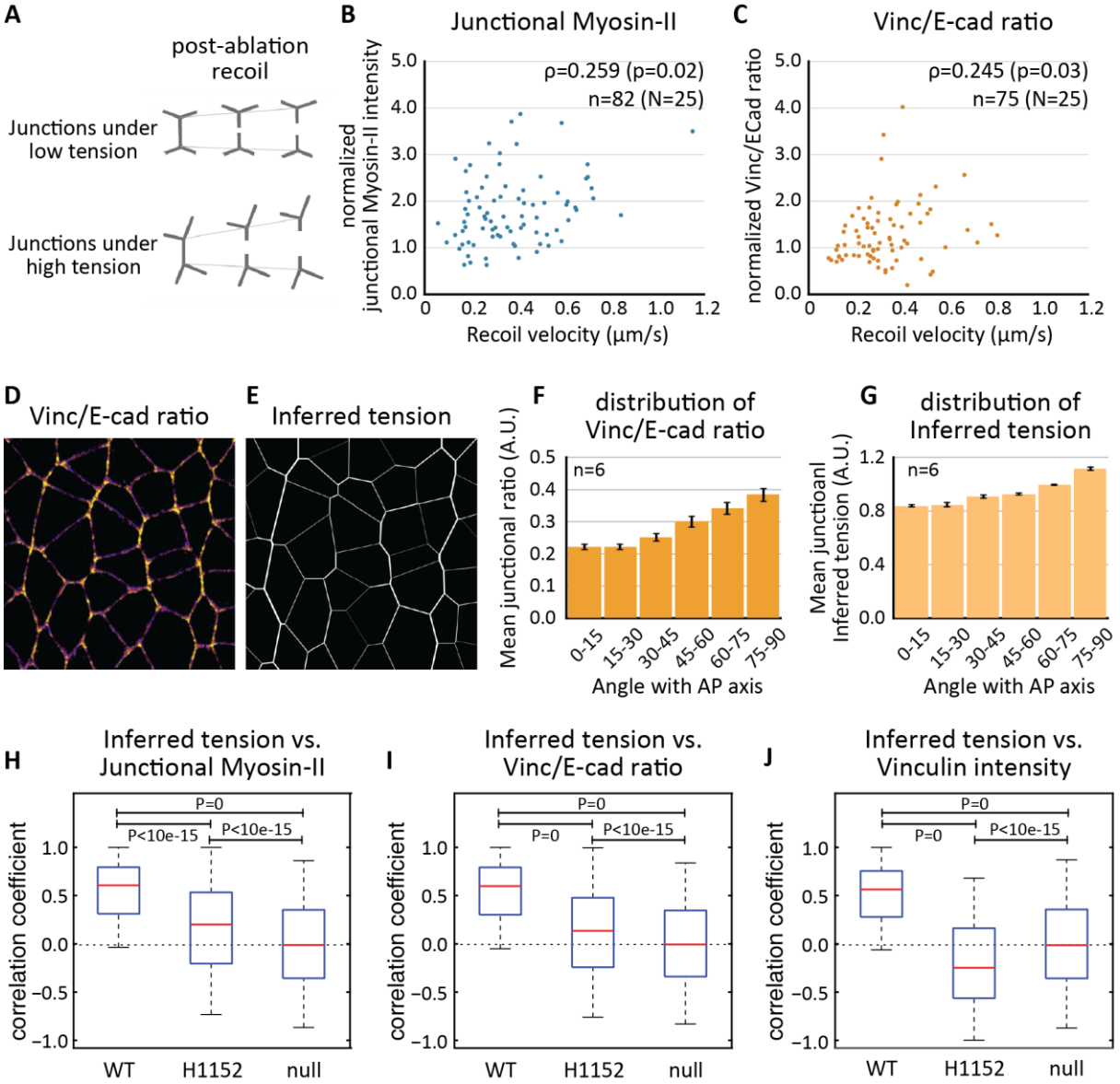

Figure3: Vinc/E-cad ratio represents the load on adhesion complexes.

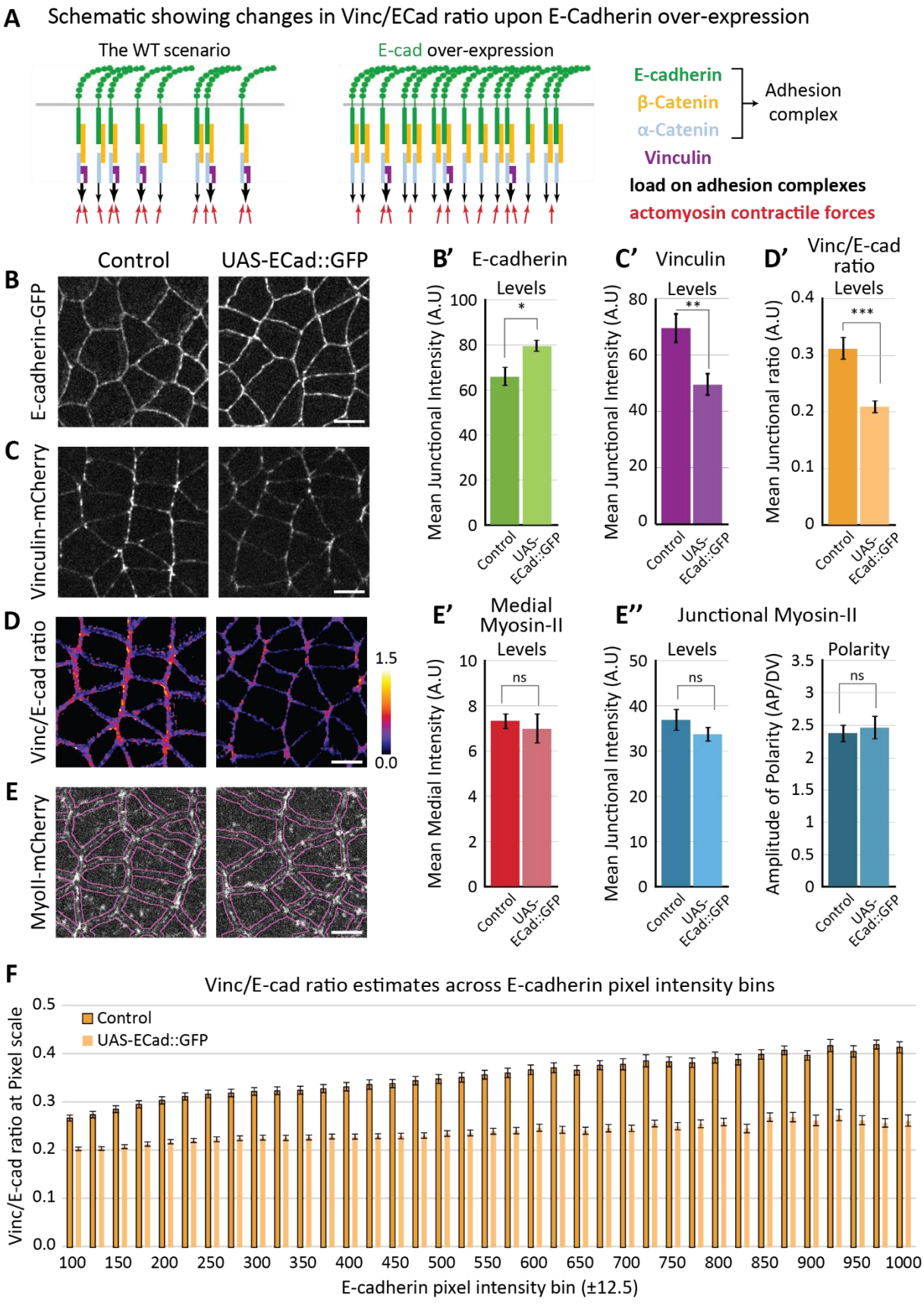

Figure4: Medial Myosin tunes the levels of Vinc/E-cad ratio, while junctional Myosin tunes its planar polarized distribution

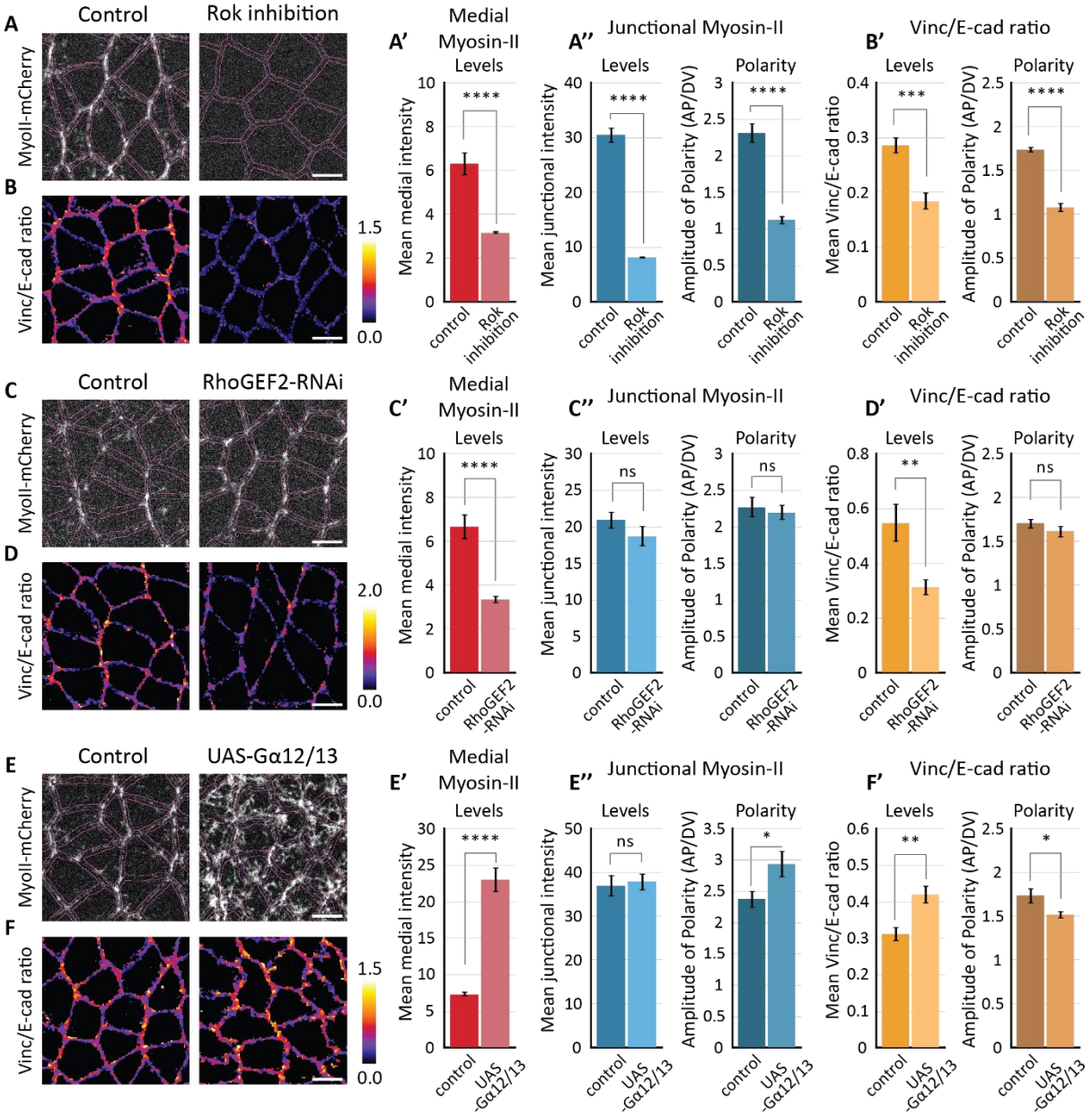

Figure5: Medial Myosin-II tunes the levels of junctional E-cadherin

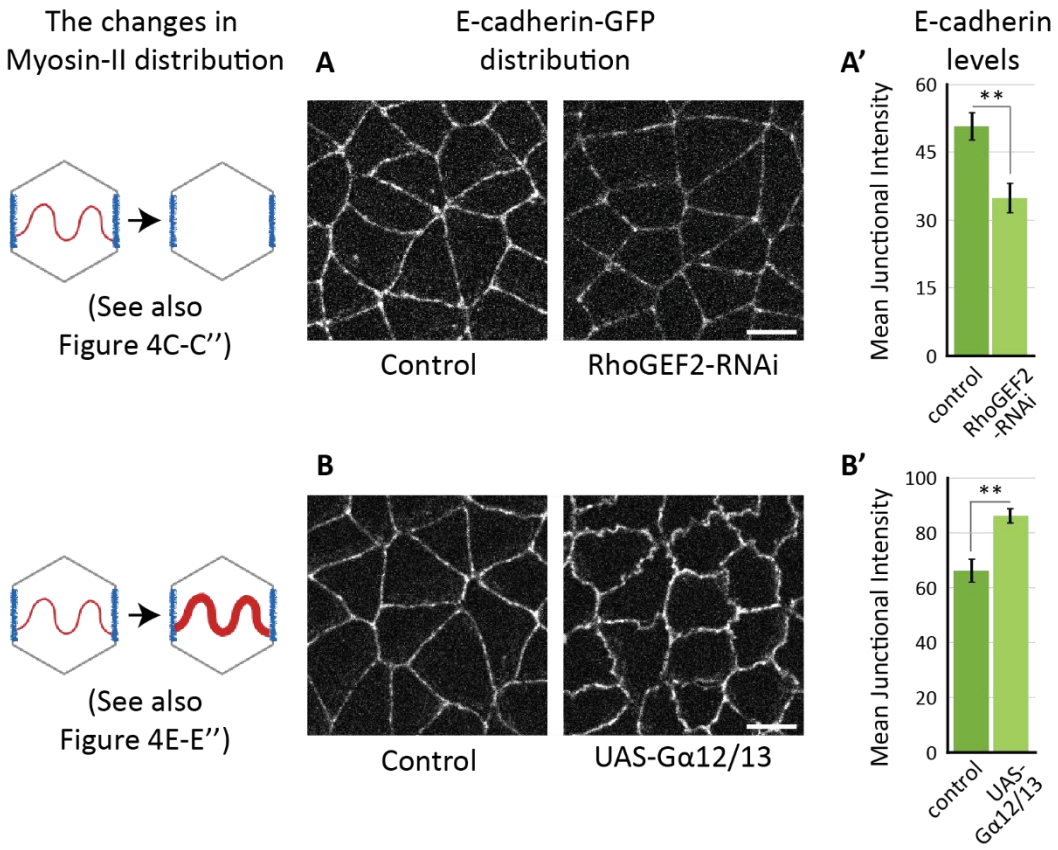
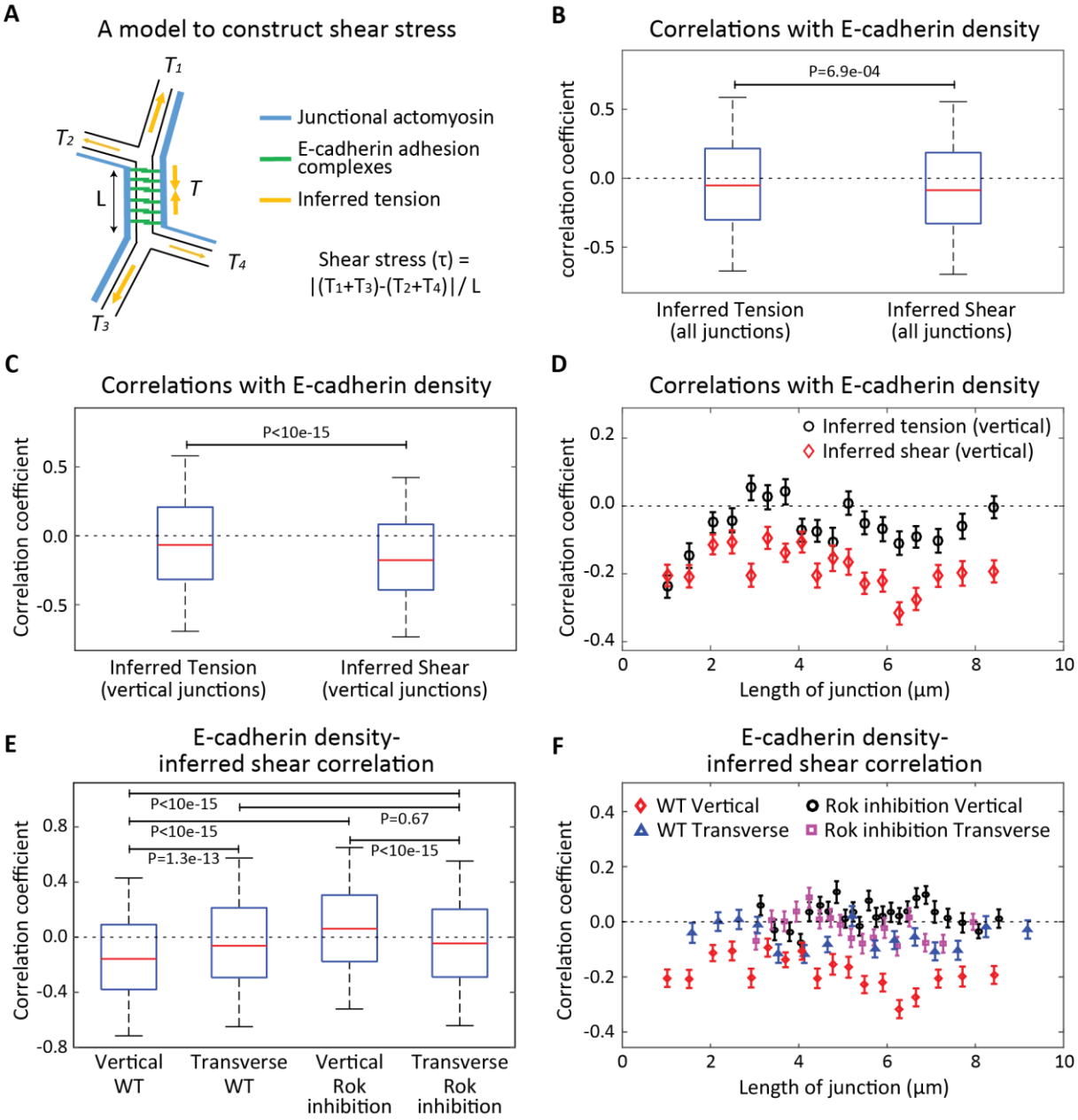
Figure6: Shear stress is negatively correlated with the levels of junctional E-cadherin